Pergamon

Cement and Concrete Research, Vol. 28, No. 2, pp. 261–270, 1998

0008-8846/98 $19.00 + .00

PII S0008-8846(97)00222-6

CONCRETE FREEZE/THAW AS STUDIED BY MAGNETIC RESONANCE IMAGING

P.J. Prado,* B.J. Balcom,[1]* S.D. Beyea,* T.W. Bremner,† R.L. Armstrong,* and P.E. Grattan-Bellew‡

MRI Centre, Department of *Physics and †Civil Engineering, P.O. Box 4400, University of New Brunswick, Fredericton, New Brunswick, Canada E3B 5A3

‡Institute for Research in Construction, National Research Council, Ottawa, Ontario, Cananda K1A 0R6

(Received June 30, 1997; in final form October 20, 1997)

ABSTRACT

A recently developed magnetic resonance imaging (MRI) technique is used to study the concrete freeze/thaw process. Ice formation is spatially resolved in a nondestructive manner as changes in the MRI signal intensity are observed. The phase transition temperatures are in agreement with published differential scanning calorimetry thermograms.

The concrete samples were air dried for varying times. The imaging of both saturated and non-saturated specimens demonstrates the ability to monitor non-adsorbed water in a range of pore sizes. The freeze/thaw thermodynamic behaviour was found to depend on water content and sample history. *© 1998 Elsevier Science Ltd*

Introduction

Concrete structures exposed to frost conditions are susceptible to deterioration caused by ice formation. Numerous studies have been undertaken to elucidate the mechanisms responsible for the frost damage. A clear goal has been the establishment of a quantitative link to moisture content, cooling rates and mix components (see for example the review by Marchand et al. (1).

Nuclear magnetic resonance (NMR) has been used to characterize water dynamics in cement paste (2–11), silica gel, and controlled-pore glass (12–14) as well as fluid transport in porous solids (15). Gummerson et al. (16) and Dickson et al. (17) have reported on the use of magnetic resonance imaging (MRI) to investigate capillary water inflow in porous materials. Furthermore, Kleinberg and Horsfield (18) and Pel et al. (19) have presented new MRI methods of observing liquids in large pores. Attard et al. (20) and Star-Lack et al. (21) reported on a MRI technique based on continuously oscillating gradients. But when researchers attempt to image water in small pores, the corresponding fast nuclear spin-spin relaxation process (tens to hundreds of μs) places a limitation on these techniques.

[1]To whom correspondence should be addressed.

We have recently developed a MRI technique, namely single-point ramped imaging with T_1 enhancement (SPRITE), which is ideally suited to space-resolved observation and characterization of water in cement pastes and concrete (22–24). The SPRITE method is based on the single-point imaging (SPI) technique (25), and has recently been used in proton density and relaxation time mapping of hardened concrete samples (26), two-dimensional imaging of concrete under thawing conditions (27), and imaging of lake bed drill cores (28).

The ability of the SPRITE technique to image water in concrete materials opens up a vast field of study in concrete research. Submillimetric resolution of moisture distribution can be achieved, whereas such resolution is obscured in γ-ray attenuation measurements (29) because of the variety of cross sections involved in heterogenous concrete samples. A novel temperature controller incorporated in the imaging system permits a space-resolved thermodynamic study of the freeze/thaw phenomena in intact specimens. In this article, these results are compared to calorimetric reports (30–32) and a critical discussion is presented.

Comments on Concrete Freeze/Thaw

A number of concrete frost damage mechanisms have been proposed and reported (1,32–44). The dynamics of ice formation in these specimens are driven by the chemical and structural properties of the material. For water-saturated hydrated cement cooled from room temperature, the first phase transition occurs at about 0°C, where the bulk and capillary-condensed water freezes. This freezing point can be lowered by up to 1.6°C, depending on the cement composition (45) or even to approximately −15°C when supercooling effects are dominant. After the bulk water has been frozen, the freezing point depression for the remaining water is related to the gel pore dimensionality by the Kelvin equation (see for example ref. 14 and 46). If the paste moisture is low enough that no evaporable water is present, the first transition may not be observed, which is the case of samples dried for several weeks under low humidity conditions.

As the temperature is lowered, additional pressure produced by ice formation and the change in relative vapor pressures for the formed solid/liquid, liquid/vapor, and solid/vapor interfaces results in water migration from small capillaries to regions where ice can now be formed. This desorption produces a secondary freezing point at about −45°C (31,42), which is superimposed on the gradual freezing determined by the pore distribution. Thereafter, some of the adsorbed water remains liquid. Evidence of structured water on the micropore walls (corresponding to two or three molecular layers) at about −90°C has been reported (39). We believe that these two low-temperature transitions are present in spite of long drying periods, whereas a non-saturated paste presents no transformation at about 0°C. As the temperature is increased, the water migration produced during freezing is not reversed and the thawing process does not present the secondary phase transition.

Although currently there is no definite agreement on the nature of the frost damage mechanism (1), the possibility of space-resolving the moisture content and ice formation in porous media in a non-destructive manner through MRI could make this type of testing a valuable tool that we believe will contribute to further understanding the concrete freeze/thaw phenomena.

TABLE 1
Concrete and mortar drying times for the freeze and thaw processes (w/c = 0.5).

Sample	Material	Curing (100% RH) days	Air Drying (40% RH) days	Process
A	concrete	3	3	freeze
B	concrete	3	5	thaw
C	concrete	3	20	thaw
D	concrete	3	21	freeze
E	mortar	3	21	freeze

Experimental

Sample Preparation

One mortar (aggregate size: under 3 mm; aggregate-to-cement proportion: 2.4) and four concrete samples were prepared with a 0.5 water-cement ratio. Samples were cylindrical, with a diameter of 50 mm and a length of 80 mm. The dimensions were chosen to ensure representative distribution of the coarse aggregates. White Portland cement (Lehigh Type 1) was used for the mix because of its low iron content (ferrite $< 1\%$). Graded quartz aggregates (Atlantic Silica Inc., Sussex N.B., Canada) with a 14-mm maximum size were added to the concrete specimens, and the final mix was vibrated for 3 s.

All samples were cured with one open face for 3 days at 100% RH, followed by air drying at room temperature at $40 \pm 10\%$ RH. The mortar and concrete samples were dried for different periods, as shown in Table 1.

For simultaneous concrete/mortar imaging, the samples were cut to 40 mm in length and placed end to end, separated by a 10-mm teflon ring. The remaining concrete cylinders were left intact. For the thawing experiments, the specimen was cooled overnight in a freezer at $-70°C$, then wrapped with insulating fibreglass and placed in a glass dewar positioned in the radio frequency (RF) probe (Figure 1).

Temperature Controller

Samples were cooled with a novel temperature controller, specially designed to fit the geometrical restriction of the imaging system. Figure 1 is a sketch of the experimental setup. A platinum resistance temperature device (RTD) on the cold nitrogen input tube was used to monitor the temperature. An Omega Series 6000, microprocessor-based controller fed pulsed current into a nitrogen dewar heater (110 V). The cold nitrogen vapor flow cooled the glass dewar (45 cm long). A thin copper-constantan thermocouple on the concrete surface was used to scan the temperature at 5-s intervals.

Sample holders and tubing in the glass chamber were made of teflon to avoid spurious proton signal during the MRI experiment. The presence of the sensor cables in the RF probe produced no detectable image distortion.

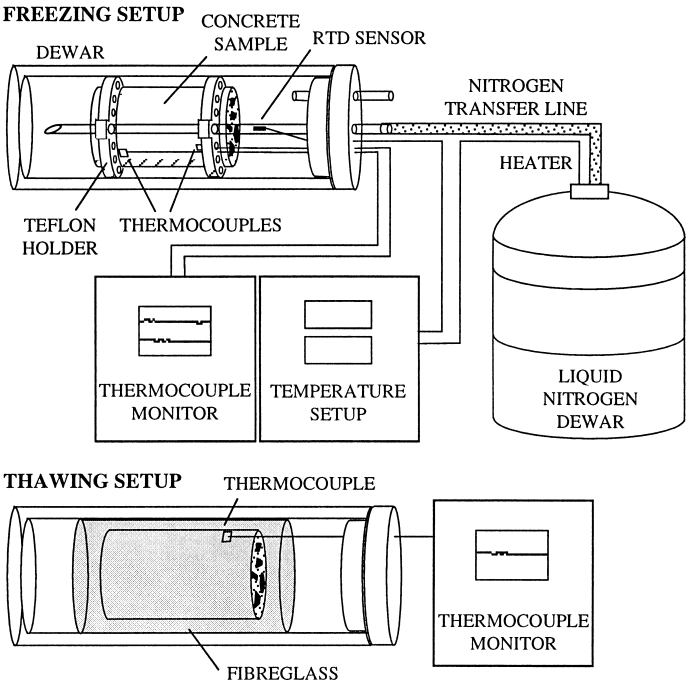

FIG. 1.
Temperature controller diagram. Freezing and thawing setup.

With this apparatus, the temperature can be held at a preset value for several hours to within 0.1°C. The cooling rate was slower than 2°C/h in all cases. A limiting rate of over 4°C/h was estimated to approach thermal homogeneity, based on the analytical solutions for the temperature evolution in cylindrical samples (47) and the concrete's thermal conductivity (~1 J/(sm°C)), density (2200 kg/m^3), specific heat (~1 kJ/(kg°C)) and coefficient of heat transfer (~60 J/(m^{2}s°C)) (48,49).

MRI Technique

Technical details of the SPRITE method have been published elsewhere (22,26,27). We summarize here some relevant aspects of the imaging process.

For a one-dimensional profile, the signal magnitude is a function of the proton density $\rho(T, x)$ and the encoding time, t_p (time at which the magnetization is detected). In SPRITE, t_p is kept constant throughout the acquisition. For our imaging parameters, the magnitude of the Fourier transformed signal defines the profile (27):

$$M(T, x) = \rho(T, x) exp\left(-\frac{t_p}{T_2^*(T, x)}\right) \quad (1)$$

T_2^* is the relaxation time (driven by the magnetic field inhomogeneities and the interaction among nuclear spins). The explicit appearance of the temperature (T) and position (x) indicates the thermal and spatial dependencies of the proton distribution and relaxation time.

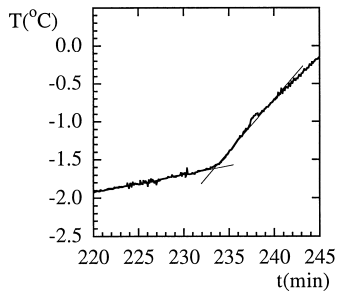

FIG. 2.
Temperature-time plot around the melting point for thawing of concrete. First order regressions are displayed.

A field of view of 14.0 cm with 64 points was determined by appropriate magnetic field gradient ($G_{max} \sim 5$ G/cm) and encoding time (105 μs). Given the investigated systems present a T_2* ranging between 60 μs and 200 μs, the chosen encoding time ensures adequate signal-to-noise at all temperatures.

The relaxation time of ice is of the order of 10 μs, which is fast for the encoding time scale and then produces no significant contribution to the signal. This permits a quantitative survey of the evaporable pore water undergoing a phase transition. Gel pore water remains liquid at the lowest studied temperatures, as reported by Jehng et al. (8).

The MRI sample parameters contain valuable information about the sample inhomogeneity, pore size distribution (1,8,9,50), and even the compressive and bending strength of a cement paste (5).

The RF probe is a 16-rod birdcage resonator (51), fed by a 2-kW RF amplifier (AMT 3445, Brea, California). Tuning was periodically checked and required no changes as the dewar interior temperature was modified. The 2.4 Tesla superconducting magnet (Nalorac Cryogenics Inc., Martinez, California) has a 32-cm horizontal bore and a water-cooled 20-cm i.d. gradient set ($G_{zmax} \approx 10$ G/cm, $G_{x,ymax} \approx 5$ G/cm). Experiments were controlled by a Tecmag (Houston, Texas) Libra S-16 console. Pulse sequence generation and data acquisition were controlled by MacNMR software based on a Macintosh Quadra 950.

Results and Discussion

For the thawing experiments with sample B, the temperature-time plot revealed that the freezing point distribution commences at about −1.5°C, as shown in Figure 2. The bi-linear shape of the plot is typical of a heat exchange effect for a melting process.

A one-dimensional moisture profile at 4°C is shown in Figure 3a and changes of this profile with temperature are displayed in a stack plot in Figure 3b.

The image intensity variation with temperature can be studied for different points along the sample. Figure 4 displays the results for the drying end and the centre of sample A, as it freezes. Values have been normalized to the high-temperature phase results, where small magnitude changes are expected to follow the Curie law (14) and the signal-to-noise ratio is increased because of maximum signal contribution. The short drying period ensured a saturated pore system with water in large and open pores.

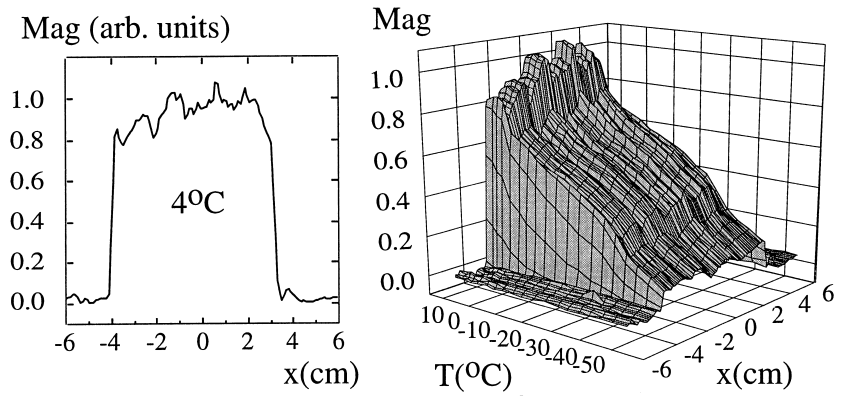

FIG. 3.

One-dimensional moisture distribution at 4°C (*a*) and stack plot of one-dimensional profiles for the freezing process (*b*). Note in (*b*) the transition regions at about −2°C and −40°C.

A heterogeneous behaviour has been previously observed for thawing conditions in a SPRITE two-dimensional analysis (27).

After drying for 3 weeks, a concrete and a mortar cylinder were cut to 40 mm in length and simultaneous concrete/mortar freezing profiles were obtained. The presence of quartz aggregates in the concrete mix reduces the overall water concentration, which is reflected in the signal intensity. The magnitudes were integrated in the regions indicated by arrows on Figure 5a and displayed as a function of the temperature in Figure 5b.

In order to assess the non-frozen water density from the signal intensity profile, the relaxation time variation should be considered (Eq. 1). T_2* values for concrete are systematically lower than for mortar (Figure 6), as a consequence of the additional inhomogeneity introduced by the coarse aggregates.

Special care has to be taken to account for changes of the signal intensity caused by an apparent phase transition (APT). This phenomenon has been described by Overloop (14) using NMR for silica gel and controlled-pore glass. Experimental evidences show that the freezing process causes a steep signal intensity change a few degrees below 0°C (determined by the Kelvin equation) and then continues to decay smoothly (no discontinuities or hysteresis effects were observed). This subsequent decay was attributed to the behaviour of water

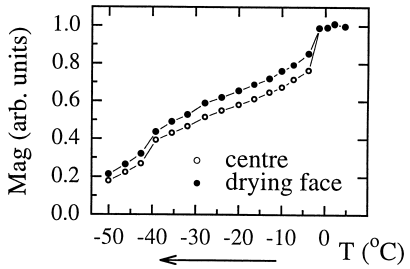

FIG. 4.

Signal magnitude evolution for two sample positions. Note the two transition ranges at about −2°C and −40°C.

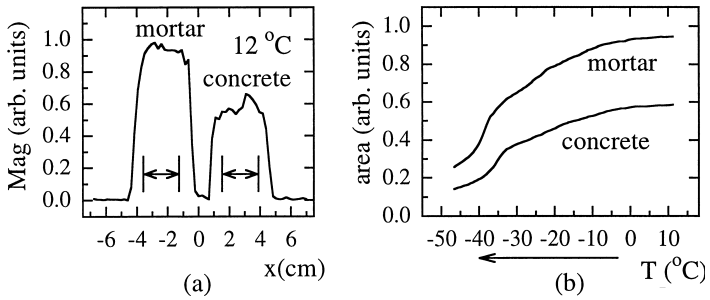

FIG. 5.
Normalized one-dimensional profile of the concrete/mortar simultaneous experiment at 12°C (*a*) and the evolution of the areas indicated by arrows (*b*).

in the first few adsorbed molecular layers (see also differential scanning calorimetry by Beddoe (37)), producing an APT. This is a feature of the NMR technique and contains no valuable thermodynamic information in the sense that this water does not acquire the structure of ice, even under the bulk water freezing point. Having considered the smooth decay for uniform pores materials, we can expect for a widely distributed pore population system the specific heat phenomena to produce pronounced changes in the magnitude plot when phase transitions occur. Then, the slope of the signal intensity is displayed and correlates with previous calorimetric results (1,30,31,37,38).

Note that the freezing rate effects on signal evolution are clearly depicted in Figure 7 and correspond to differential scanning calorimetry thermograms of cement pastes. The exothermic heat of the main and secondary transition appear as sudden changes in the intensity slope.

Figures 7a and 7b correspond to samples A and B, with high moisture content. The moisture content is lower for samples C, D, and E, generating a poorer signal-to-noise ratio (seen in the normalized plots for samples D and E). Under thawing conditions, sample B and C presented similar slope behaviour. As the water contained in the bigger pores evaporated first, the main transition tends to vanish (see freezing results in Fig. 7c vs. Fig. 7a). This feature is also depicted in Figure 7a, where the drying phase shows a less dramatic change at about −2°C, when compared to the centre of the sample. Furthermore, the process is accompanied by a small peak at approximately −30°C, which is a result of the ambient humidity (42), thus more pronounced at the open face of the sample.

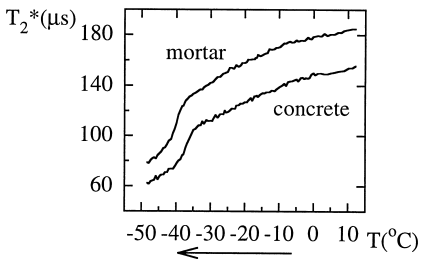

FIG. 6.
Signal free induction decay time, T_2*, for the concrete/mortar freezing process.

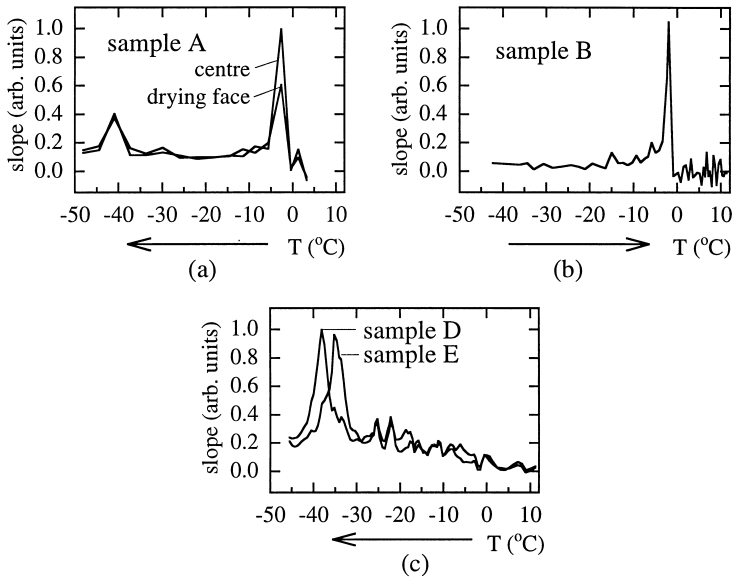

FIG. 7.
Slope of the magnitude vs. temperature curve for the freezing and thawing experiments. Phase transitions and evaporable water contents are depicted. All plots are normalized by their maximum amplitude.

Figure 7c indicates that the secondary transition occurs at a slightly lower temperature in concrete than in mortar.

The space resolved analysis can be extended to two- and three-dimensional SPRITE. A two-dimensional study of the thawing process has been reported (27).

Concluding Remarks

The use of the SPRITE imaging method in a series of concrete samples with different drying conditions has established the possibility of studying water phase transitions in a new manner that permits analysis as a function of position. Changes of signal intensity with temperature were used to monitor the relative amount of freezable water and stressed the dependencies on local water content. The transition temperatures are consistent with previous differential scanning calorimetry results.

MRI, through its sensitivity to freeze/thaw, is a potential tool for investigating concrete deterioration under frost conditions. Furthermore, the water molecule behaviour and inherent heterogeneity of concrete makes it an ideal subject for the SPRITE method. The thermodynamic analysis presented here can be performed on small regions of a concrete specimen and can be extended to three dimensions.

Acknowledgments

We thank NSERC of Canada for operating (BJB) and equipment (BJB, RLA) grants. This work was supported by an NSERC/NRC Research Partnership award (BJB, RLA, TWB).

References

1. J. Marchand, R. Pleau and R. Gagné, Material Science of Concrete IV, p. 283, Am. Ceram. Soc, Westerville, 1995.
2. K.S. Mendelson, W.P. Halperin, J.-Y. Jehng, and Y.-Q. Song, Magn. Reson. Imaging 12, 207 (1994).
3. K.S. Mendelson, Phys. Rev. B 47, 1081 (1993).
4. S. Stapf, Kimmich and R.-O. Seitter, Magn. Reson. Imaging 14, 841 (1996).
5. R. Blinc, J Dolinsek, G. Lahajnar, A. Sepe, I. Zupancic, S. Zumer, F. Milia, and M.M. Pintar, Z. Naturforsch. 43a, 1026 (1988).
6. M. Peyron, G.K. Pierens, A.J. Lucas, L.D. Hall, and R.C. Stewart, Magn. Reson. Imaging 14, 214 (1996).
7. J.H. Strange, S.G. Allen, P.C.L. Stephenson, and N.P. Matveeva, Magn. Reson. Imaging 14, 963 (1996).
8. J.-Y. Jehng, D.T. Sprague, and W.P. Halperin, Magn. Reson. Imaging 14, 785 (1996).
9. E. Laganas, G. Papavassiliou, M. Fardis, A. Leventis, F. Millia, E. Chaniotakis, and C. Meletiou, J. Appl. Phys. 77, 3343 (1995).
10. W.P. Halperin, J.-Y. Jehng, and Y.-Q. Song, Magn. Reson. Imaging 12, 169 (1994).
11. G.C. Borgia, R.J.S. Brown, and P. Fantazzini, J. Appl. Phys. 79, 3656 (1996a).
12. F. D'Orazio, J.C. Tarczon, W.P. Halperin, K. Eguchi, and T. Mizusaki, J. Appl. Phys. 65, 742 (1989).
13. K. Overloop and L. Van Gerven, J. Magn. Reson., Series A 101, 147 (1993).
14. K. Overloop and L. Van Gerven, J. Magn. Reson., Series A 101, 179 (1993).
15. K.J. Packer and J.J. Tessier, Molec. Phys. 87, 267 (1996).
16. R.J. Gummerson, C. Hall, W.D. Hoff, R. Hawkes, G.N. Holland, and W.S. Moore, Nature 281, 56 (1979).
17. M.L. Dickson, T.T. Tucker, and E.J. Fernandez, AIChE J. 43, 409 (1997).
18. R.L. Kleinberg and M.A. Horsfield, J. Magn. Reson. 88, 9 (1990).
19. L. Pel, K. Kopinga and H. Brocken, Magn. Reson. Imaging 14, 931 (1996).
20. J.J. Attard, P.J. McDonald, S.P. Roberts, and T. Taylor, Magn. Reson. Imaging 12, 355 (1994).
21. J.M. Star-Lack, M.S. Roos, S.T.S. Wong, V.D. Schepkin, and T.F. Budinger, J. Magn. Reson. 124, 420 (1997).
22. B.J. Balcom, R.P. MacGregor, S.D. Beyea, D.P. Green, R.L. Armstrong, and T.W. Bremner, J. Magn. Reson., Series A 123, 131 (1996).
23. M. Bogdan, B.J. Balcom, T.W. Bremner, and R.L. Armstrong, J. Magn. Reson., Series A 116, 266 (1995).
24. D.E. Axelson, A. Kantzas, and T. Eads, Can. J. Appl. Spectrosc. 40, 16 (1995).
25. S. Emid and J.H.N. Creyghton, Physica B 128, 81 (1985).
26. S.D. Beyea, B.J. Balcom, P.J. Prado, R.L. Armstrong, and T.W. Bremner, J. Magn. Reson. submitted.
27. P.J. Prado, B.J. Balcom, S.D. Beyea, R.L. Armstrong, and T.W. Bremner, Solid State NMR, submitted.
28. F.R. Rack, B.J. Balcom, R.P. MacGregor, and R.L. Armstrong, J. Limnology, Special Issue on Lake Winnipeg, submitted.
29. M.K. Kumaran and M. Bomberg, Proceedings International Symposium on Moisture and Humidity, NRCC DBR Paper 1302, Washington, DC, 485 (1985).
30. D.H. Bager and E.J. Sellevold, Cem. Concr. Res. 16, 709 (1986).
31. S. Jacobsen, H.C. Gran, E.J. Sellevold, and S. Matala, Cem. Concr. Res. 26, 919 (1996).
32. M.T. Leivo, Nordic Concrete Research, p. 142, Norske Betongforening, Oslo, 1989.
33. G.G. Litvan, ACI J. 82–66, 724 (1985).

34. G.G. Litvan, Proceedings RILEM/IUPAC International Symposium on Pore Structure and Properties of Materials, Prague, 1973.
35. R.J. Detwiler, B.J. Dalgleish, and R.B. Williamson, ACI Mater. J. 86-M4, 29 (1989).
36. S. Jacobsen, E.J. Sellevold, and J.A. Bakke, Cem. Concr. Res. 25, 1775 (1995).
37. R.E. Beddoe and M.J. Setzer, Cem. Concr. Res. 20, 236 (1990).
38. R.E. Beddoe and M.J. Setzer, Cem. Concr. Res. 18, 249 (1988).
39. F. Radjy and E.J. Sellevold, Nature Phys. Sci. 241, 133 (1973).
40. P.E. Grattan-Bellew, Const. Build. Mat. 10, 3 (1996).
41. G.G. Litvan, J. Am. Ceram. Soc. 58, 26 (1975).
42. G.G. Litvan, J. Am. Ceram. Soc. 55, 38 (1972).
43. S. Chatterji, Cem. Concr. Res. 15, 13 (1985).
44. H. Newlon and T.M. Mitchell, Significance of tests and properties of concrete and concrete-making materials, p. 153, ASTM, Philadelphia, 1993.
45. T.C. Powers and T.L. Brownyard, J. Am. Concr. Inst. 18, 934 (1946).
46. J.H. Strange, J.H. Webber, and S.D. Schmidt, Magn. Reson. Imaging 14, 803 (1996).
47. W.H. McAdams, Heat Transmission, p. 41, McGraw-Hill, New York, 1954.
48. A.M. Neville, Properties of Concrete, Longman Scientific & Technical, UK, 1994.
49. W.M. Rohsenow and H.Y. Choi, Heat, Mass, and Momentum Transfer, Prentice-Hall, Inc, Englewood Cliffs, 1961.
50. G.C. Borgia, V. Bortolloti, P. Dattilo, P. Fantazzini, and G. Maddinelli, Magn. Reson. Imaging 14, 919 (1996b).
51. C.E. Hayes, W.A. Edelstein, J.F. Schenck, O.M. Mueller, and M. Eash, J. Magn. Reson. 63, 622 (1985).